Metal–Organic Framework Photonic Balls: Single Object Analysis for Local Thermal Probing

Civan Avci, Maria Letizia de Marco, Caroline Byun, Jonathan Perrin, Mario Scheel, Cedric Boissiere, Marco Faustini

Metal-Organic Framework Photonic Balls: Single Object Analysis for Local Thermal Probing

Civan Avci,[1] Maria Letizia De Marco,[1] Caroline Byun,[1] Jonathan Perrin,[2] Mario Scheel[2], Cédric Boissière,[1] Marco Faustini[1*]

1 Sorbonne Université, CNRS, Laboratoire Chimie de la Matière Condensée de Paris (LCMCP), F-75005 Paris, France

2 *Synchrotron Soleil, 91192 Gif-sur-Yvette, France*

Keywords: Metal-Organic Frameworks, Photonics, Spray-Drying, Thermal, Hyperspectral Microscopy

Abstract

Due to their high porosity and chemical versatility, metal–organic frameworks exhibit physical properties appealing for photonic-based applications. While several MOF photonic structures have been reported, examples of applications of are mainly limited to chemical sensing. Herein, we extend the range of application of photonic MOFs to local thermal and photothermal sensing by integrating them into a new architecture: MOF photonic balls. Micrometric-sized photonic balls are made of monodispersed MOFs colloids that are self-assembled via spray-drying, a low-cost, green and high-throughput method. The versatility of the process allows tuning the morphology and the composition of photonic balls made of several MOFs and composites with tailored optical properties. X-Ray Nanotomography and Environmental Hyperspectral Microscopy enable analysis of single objects and their evolution in controlled atmosphere and temperature. Notably, in presence of vapors, the MOF photonic balls act as local, label-free temperature probes. Importantly, compared to other thermal probes, the temperature detection range of these materials can be adjusted "on-demand". As proof of concept, the photonic balls were used to determine local temperature profiles around a concentrated laser beam. More broadly, this work is expected to stimulate new research on the physical properties of photonic MOFs providing new possibilities for device fabrication.

Table of Contents

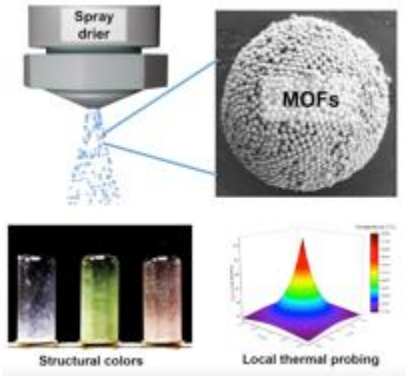

Metal Organic Framework Photonic Balls are fabricated by self-assembly of MOFs colloids into microdroplets via spray-drying, a low-cost, green and high-throughput method. The versatility of the process allows tuning the morphology and the composition of materials with tailored photonic properties. We demonstrate that the MOF photonic balls can act as local, label-free (photo) thermal probes that enable determination of sub-millimetric temperature gradients.

1. Introduction

Probing of the local temperature at the sub-millimeter scale is an important challenge with implications in many domains such as microelectronics,[1–3] photonics,[4,5] biology[6–8] or engineering.[9–11] Currently, thermal imaging at the macroscale is done with the well-established infrared (IR) imaging technology. However, going down to the microscale imaging becomes complicated since the spatial resolution is intrinsically limited by the IR wavelength. In addition, the currently used methods require expensive instruments. A straightforward approach consists in using thermally sensitive probes such as fluorescent molecules or particles[12–18] including lanthanide-based metal-organic frameworks (MOFs).[19–22] Based on temperature dependent fluorescence variations, several techniques such as fluorescence anisotropy microscopy,[23,24] fluorescence microscopy,[3,18,25] and fluorescence intensity[26–28] were developed. While fluorescent probes are successfully used as micro- and nano-thermometers, their synthesis is often challenging and multi-step. In addition, they can suffer from stability issues and their utilization is limited to not-fluorescent supports or environments. For these reasons, the development of alternative materials acting as label-free thermal probes is of high interest in the field of thermal measurement. To design a new label-free, thermal-optical probe, we set a certain number of requirements: (i) its transduction mechanism should be compatible with an optical microscopy to allow mapping (ii) it should present high thermal sensitivity and versatility (iii) The probe should be prepared by low-cost, environmentally friendly and high throughput synthetic methods compatible with industrial production.

The emergence of nanoporous materials such as MOFs with tailored chemical and physical properties offers new opportunities to design devices with new functionalities.[29–33] Because of their capability in hosting guest molecules into their cavities, MOFs are widely employed in a number of domains including gas storage and energy,[34–39] catalysis[40–46] and, to a lesser extent, optics.[47–49] To be used in optical applications, MOFs were integrated into optical structures such as Fabry-Pérot devices,[50–52] plasmonic composites,[53–55] Bragg Mirrors,[56,57] 2D diffraction gratings,[58–60] 3D photonic crystals and monoliths[61] or photonic glasses.[62] In all the above-mentioned cases, the only practical utilization was essentially limited to chemical sensing in gas or liquid media.[63] In this context, MOFs were used as sensitive medium since their refractive index varies when a vapor molecule is adsorbed into the porosity. This optical change depends on the concentration of the molecule in the atmosphere but also on the temperature of the porous matrix. This relatively simple assumption brings to

light that in presence of a controlled pressure of vapor, MOFs can be considered as thermo-optical materials. Apart from that, while a promising temperature-to-optical transduction can be envisioned, another challenge concerns the shaping as optical probe. The previously reported optical structures are films or monoliths that are continuous but not discrete objects thus; they are not adapted to act as local temperature probes. One promising family of structure are photonic balls that are discrete micrometric sized objects exhibiting structural colors. Photonic balls showing opal or inverse opal structures have been made from colloidal polymers, SiO_2 and TiO_2.[64–73] While some elegant self-assembled MOF spherical superstructures have been reported,[74–76] fabrication of MOF photonic balls has not been attempted so far.

In this study, we produce MOF photonic balls by costless and high throughput spray-drying method. MOF photonic balls are discrete microscale photonic crystals in pseudo-spherical shapes made of colloidal MOF particles. Here, we mainly target ZIF-8 colloids because of their stability and sharp sorption capabilities. Additionally, to prove the versatility of the approach, we also extended the same process to fabricate ZIF-67 and ZIF-8/Au nanoparticles composite photonic balls. A set of characterization techniques such as Transmission X-ray Microscopy (TXM) and X-Ray Nanotomography or Scanning Electron Microscopy (SEM) and Environmental Hyperspectral Microscopy enables both structural and optical characterizations of the materials at the single object level. We demonstrate that in presence of vapor, the MOF photonic balls act as local, label-free temperature probes that can be used on a wide range of surfaces. With respect to the other thermal probes, the temperature detection range of these MOF photonic thermal probes can be adjusted "on-demand" by controlling the partial vapor pressure in the surrounding atmosphere. As proof of concept of application, these materials are used to determine local temperature profiles of "hot-spots" caused by photothermal effect of a concentrated laser beam. Beyond the original fabrication of these hierarchical structures, this work extends the range of applications of photonic MOFs to new domains such as thermal imaging or even smart photonic pigments.

2. Results and Discussion

The fabrication approach of MOF photonic balls is illustrated in **Figure 1a**. First, we synthesized colloidal polyhedral ZIF-8 particles via a method reported elsewhere.[61] ZIF-8 is a prototypical MOF made of Zn(II) ions and 2-methylimidazole (2-mim) linkers with a reported specific surface area ranging from 1200 to 1600 m^2/g. It is known for its production in the colloidal form at very high particle size and shape monodispersity, making it suitable

for photonic and self-assembly applications.[61,77,78] In particular, we take inspiration from a recently reported synthesis of monodisperse ZIF-8 particles forming highly ordered and densely packed superstructures under fast evaporation conditions.[61,78] In this work, we processed the colloidal solution by spray drying, a well-known method in which the solution is sprayed through a nozzle to form micro-droplets that are almost instantaneously dried by an injected hot air. Each droplet forms a micrometric sphere.[79–85] Notably, this method is liquid waste-free, most part of time based on aqueous solution, and it allows easy scale-up from lab to industrial scale.[86–88] In our work, we hypothesized that the colloidal self-assembly of monodisperse ZIF-8 particles can be confined into micro-droplets to yield ordered spherical microstructures by spray drying. To verify this, in a first set of experiments, we synthesized highly monodisperse ZIF-8 particles in three sizes (colloid size, φ = 184, 206 and 242 nm) and dispersed them in water at a concentration of 30 mg ml^{-1}. The ZIF-8 colloidal solution was then spray dried with a rate of 3 ml/min in hot air and the resulting powder was collected in a vial. All powders obtained by this way were already slightly colored. Since ZIF-8 is not absorbing in the visible range, this observation represents a first indication of the presence of a structural color. X-Ray diffraction (XRD) and N_2 physisorption analyses confirmed that our material is composed of highly crystalline ZIF-8 particles and have a BET surface area of 1586 m^2/g (**Figure S1** and **S2**, **Supporting Information**) characteristic of a microporous materials with a pore size of 1.1 nm in accordance with the reported values.[89] Their morphologies were first characterized by SEM. The SEM images (**Figure 1b-e, Figure S3, Supporting Information**) of these powders revealed the formation of the micrometric photonic balls made of ordered self-assembled ZIF-8 colloids. We observed that the photonic balls are not perfectly spherical but exhibit a pseudo-spherical shape with a log-normal size distribution centered at 9 ± 5 µm (standard deviation = 5 µm, extremes range from 2 to 21 µm). The polydispersity is typical of spray drying devices using atomization nozzles based Rayleigh instabilities processing, and can be attributed to the polydisperse size distribution of the micro-droplets prior to drying. Although spray-dried particles are not always perfectly spherical (due sometimes to buckling or crumpling effects),[82] their external surface is smoothly curved. The pseudo-sphericity observed here is very unusual and it is due to the tendency of the polyhedral particles to self-assemble in the densest packing possible. Interestingly, faceted superstructures were observed in the photonic balls produced with the largest particle size (242 nm) (**Figure 1d** and **Figure S4**, **Supporting Information**). It is known from previous reports[61,78] that ZIF-8 polyhedral particles self-assemble into their densest packing, in Bravais lattices such as rhombohedral or face-centred cubic. The faceted

polyhedral particles have a higher tendency to form flat surfaces (as respect to spherical colloids for instance) at the liquid/air interface. In a confined volume, such as a micro-droplet, the competition between the surface energy of the droplet (which favors the curved surfaces) and the crystallization energy of the colloids (which favors faceted superstructures) becomes crucial. This competition is influenced by curvature radius (size of the droplets) and by the size of the colloids. As general tendency, it is thus expected that large droplets with small colloids will favor curved surfaces while small droplets with big colloids will favor more faceted superstructures.

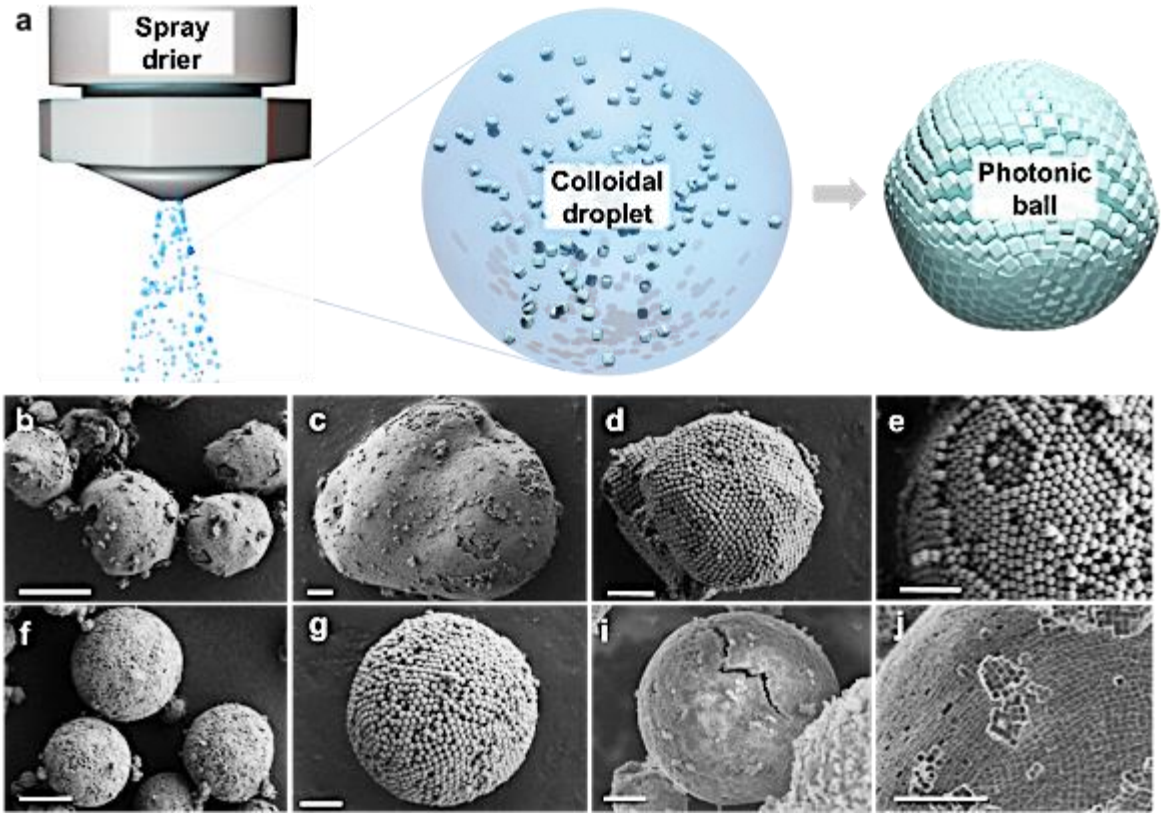

Figure 1. Morphology of the MOF photonic balls. **a)** Scheme of the self-assembly of MOF photonic balls via spray drying and SEM micrographs of various photonic balls: **b)** a general view of ZIF-8 photonic balls (φ = 242 nm) **c)** a single ZIF-8 photonic ball (φ = 206 nm) and **d)** φ = 242 nm, **e)** a closer view of a ZIF-8 photonic ball exhibiting ordered particles (φ = 184 nm), **f)** a general view of ZIF-8/PVA photonic balls (φ = 275 nm), **g)** a single ZIF-8/PVA photonic ball (φ = 275 nm), **i)** a single ZIF-67 photonic ball (φ = 205 nm) and **j)** a closer view to the underlying ordered self-assembly. Scale bars: 10 µm for **b** and **f**; 2 µm for **c**, **d**, **g**, **i** and **j**; 1 µm for **e**.

This deformed/faceted morphology and the polydispersity in size is not necessarily a drawback when optimizing the photonic properties, as we will further discuss later on.

The sphericity of the photonic balls was improved by adding a low amount of polyvinyl alcohol (PVA) in the ZIF-8 colloidal solution (1% wt prior to ZIF-8). SEM micrographs show that the balls containing ZIF-8 particles (φ = 275 nm) and PVA present a spherical shape conserving a certain structural colloidal ordering (**Figure 1f,g**) and photonic colors (as discussed later on). The versatility of the approach based on spray drying was proved by extending the fabrication scheme to other optically relevant systems. In a first example, gold plasmonic nanoparticles having size of 51 nm were added to the ZIF-8 colloidal solution to obtain composite plasmonic/photonic balls as shown in the SEM micrographs (**Figure S5, Supporting Information**). In a second example, we adapted the spray drying approach to fabricate photonic balls made of ZIF-67 particles (φ = 193 nm and 205 nm) as shown in SEM micrographs in **Figure 1i,j**. To do so, we developed a protocol strategy to synthetize monodisperse ZIF-67 colloids. XRD and N_2 physisorption analyses confirmed that our material is composed of highly crystalline porous ZIF-67 particles and have a BET surface area of 1112 m^2/g (**Figure S6** and **S7**, **Supporting Information**) in accordance with the reported values.[90] Interestingly, these materials can combine the photonic colors due to the presence of the self-assembled superstructures with the intrinsic color that results from the strong absorption of Co species in ZIF-67. To gain further insights on the inner structure of the balls we performed X-ray Nanotomography using the TXM of Anatomix beamline in Zernike phase contrast. As respect to electronic tomography, this technique is performed at ambient atmosphere and is well suited to image fragile biological samples or organic materials down to a resolution of about 100 nm. Here, for the first time, we propose to exploit of X-ray Nanotomography to characterize MOFs; this method based on X-Ray enables 3D reconstruction of the photonic balls without collapse of the microstructure of the MOFs. The methodology that is previously reported,[91,92] is adapted for analyzing our MOF photonic balls (**Figure 2a**). Briefly, individual balls are immobilized on the top of a metallic needle. TXM radiography images of MOF balls are taken while rotating the needle through a motorized stage. Then, each series of micrographs enables volume reconstruction and allows visualizing the photonic balls in 3D to observe their inner structure (**Figure 2b**). **Figure 2c** shows a vertical slice through the reconstructed volume of typical ZIF-8 photonic ball. As mentioned above, the object is not completely spherical but is faceted as a result of the surface self-assembly of the polyhedral colloids.

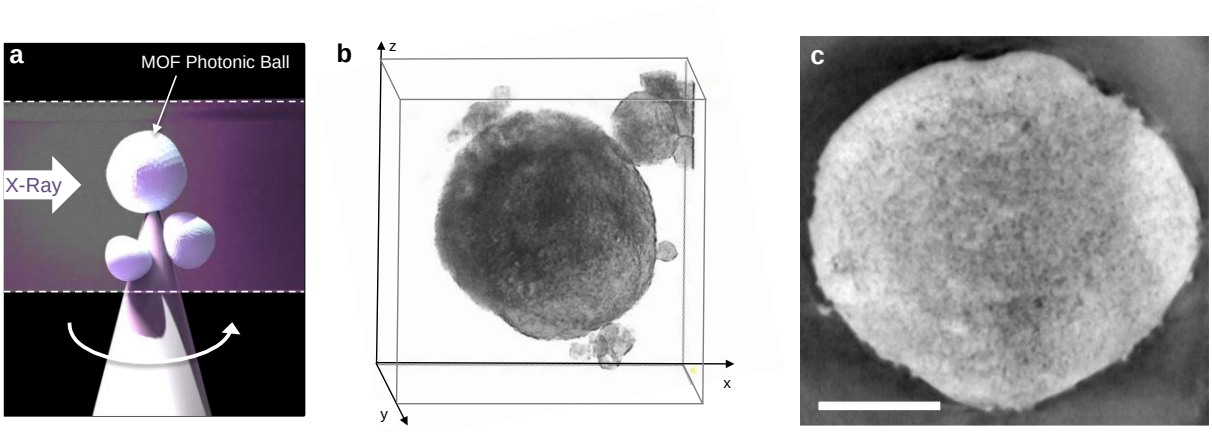

Figure 2. X-Ray Nanotomography of MOF photonic balls. **a)** Illustration of the X-Ray Nanotomography set-up; **b)** 3D rendered view of a reconstructed volume a ZIF-8 photonic ball; **c)** Vertical slice of the 3D volume of a ZIF-8 photonic ball, Scale bar: 5 µm.

The TXM micrographs of a large number of objects revealed that most of the ZIF-8 photonic balls were full inside (**Figure S8, Supporting Information**). We also observed from TXM radiographs and SEM micrographs of fractured photonic balls, that some objects are hollow superstructures having an ordered wall consisting of at least 4-5 layers of particles (**Figure S9**, **Supporting Information**). For physico-chemical reasons, hollow spheres often obtained by spray drying of suspensions of large colloids, as shown and discussed more in details in previous reports.[82] The quality of the self-assembly in the case of hollow spheres was investigated by SEM in the case of broken spheres (Figure S8). In all the cases, the ZIF-8 colloids that form the wall of the hollow balls are assembled in a closed-packed configuration, indicating that the hollow character does not seem to affect the quality of the self-assembly.

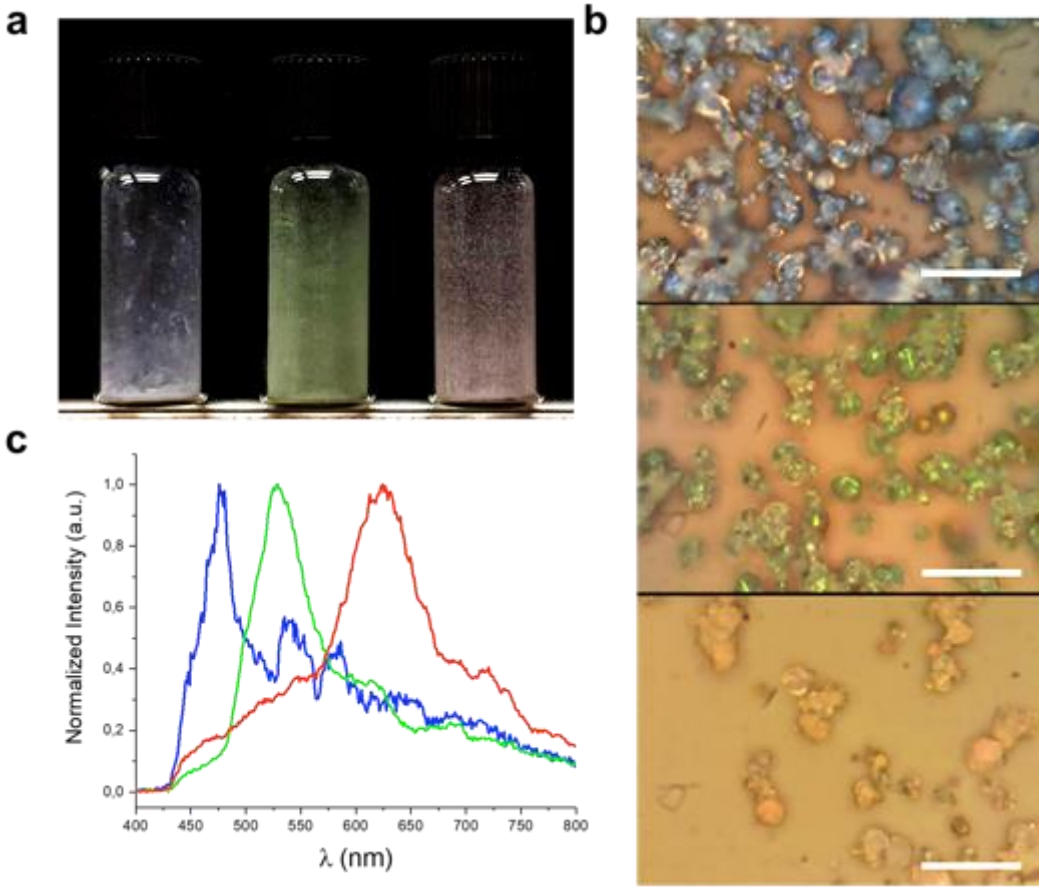

Figure 3. ZIF-8 photonic balls in different colors. **a)** Photograph, **b)** OM images, scale bar: 50 µm, and **c)** reflection spectra of the ZIF-8 photonic balls in three (blue, green and red) colors having φ = 184, 206 and 242 nm and photonic bands centered at 476, 533 and 624 nm, respectively.

After morphological and structural characterizations, we investigated the optical properties of the ZIF-8 photonic balls. All the ZIF-8 colloidal solutions were initially milky white. As mentioned above, depending on the size of the colloidal particles, faint blue, green and red colored powders were obtained after the spray drying process. To reduce the intrinsic scattering of the materials and to further enhance the naked eye visibility of the photonic colors, a slight amount of carbon black (5 w% prior to ZIF-8) was added into the ZIF-8 colloidal solutions before spray drying. In all cases, photonic colors of the three dry samples were then clearly visible with naked eyes (**Figure 3a**) and by optical microscopy (OM) (**Figure 3b**). SEM micrographs at different magnification of the three systems are reported in Figure S3. In these OM images, the photonic balls having different size and shape are clearly distinguishable. The photonic reflections were observed as a bright region positioned randomly on the photonic balls. These bright regions were attributed to the flat surfaces

allowing stronger reflections in comparison with the curved surfaces. Importantly, all the balls of each series exhibit structural colors. Reflection spectra of these blue, green and red photonic balls show characteristic peaks attributed to the photonic bands centered at 476, 533 and 624 nm, respectively (**Figure 3c**).

The photonic properties of each individual ball were characterized by environmental hyperspectral microscopy as shown in **Figure 4a**. The microscope is equipped with a spectrometer and a piezoelectric scanner, which moves the sample stage along the y-axis in order scan the sample by collecting multiple spectra on a single region of interest. This feature allowed us to collect hyperspectral images of the ZIF-8 photonic balls (**Figure 4a inset** and **Figure 4b**) and to reveal the optical properties of any selected region where each pixel of a hyperspectral image corresponds to a raw reflection spectrum. In our hyperspectral images, most of the photonic balls look dark. It is important to specify that the different appearances observed between hyperspectral and classical optical images (such as **Figure 4b** versus **Figure 3b**) are due to the acquisition mode, not to the materials. The hyperspectral images are not taken directly by a camera but results from a reconstruction of the raw reflection spectra (not normalized by the spectrum of the lamp) of each pixel whose appearance can be modified arbitrarily. This method enables, for example, acquisition of hyperspectral images of the photonic balls on a surface at 10X magnification; the photonic band of each photonic ball is thus investigated separately to quantify the "optical homogeneity" of our materials. In the example shown here, we selected randomly fourteen individual ZIF-8 photonic balls spread over the entire sample (**Figure 4b, left**) and plotted their reflection spectra in superposition. The result revealed that all of the fourteen ZIF-8 photonic balls possess a photonic band with a similar narrowness, centered at 533 ± 5 nm, showing that they exhibit a homogeneous optical quality throughout the entire powder. (**Figure 4b, right**).

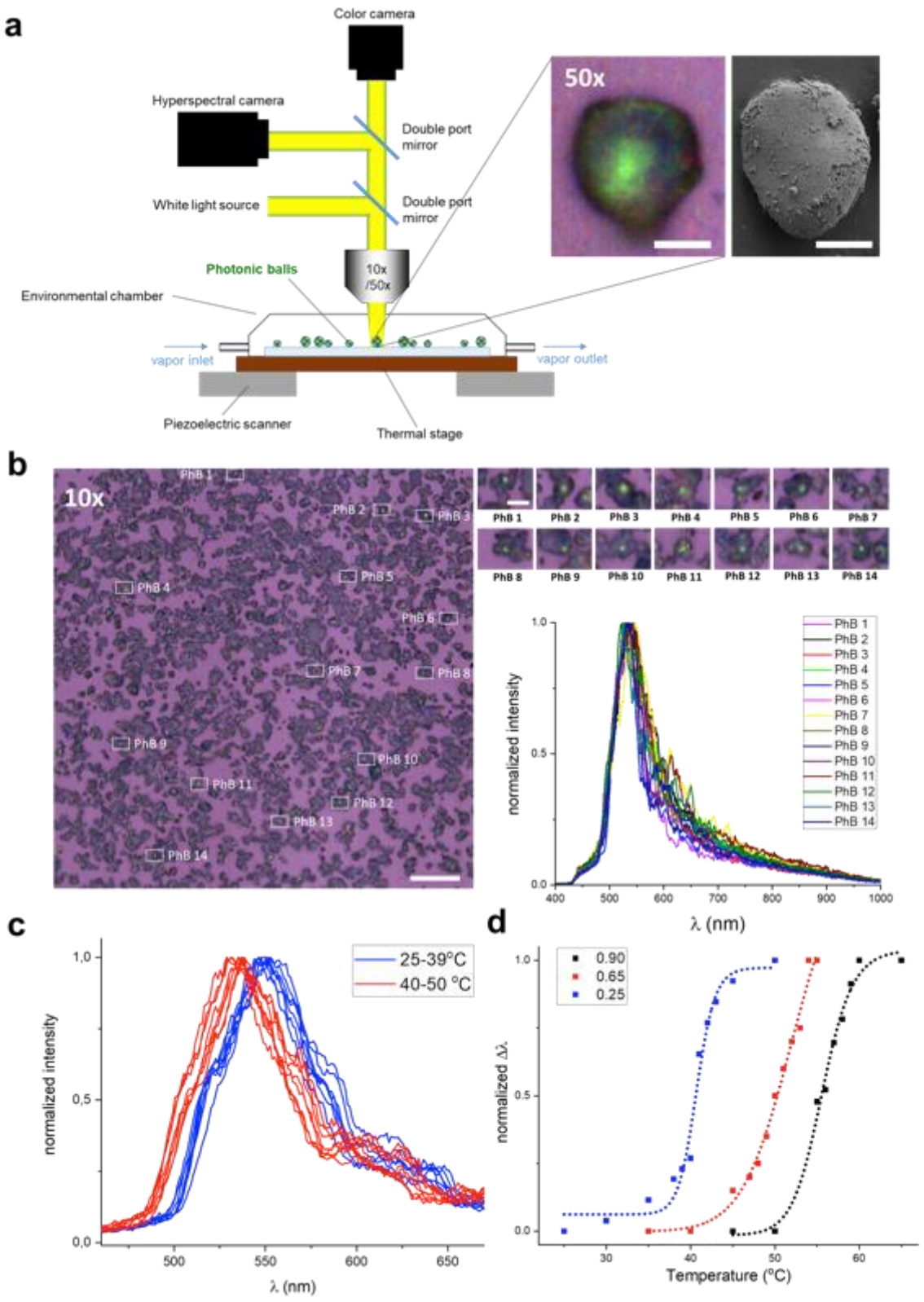

Figure 4. Optical characterization of the ZIF-8 photonic balls. **a)** Scheme of hyperspectral microscope (left), a representative hyperspectral (right) and SEM image of a ZIF-8 photonic ball, scale bar: 5 µm. **b)** Hyperspectral image of ZIF-8 photonic balls at 10X magnification with fourteen individual photonic balls (PhB1 to PhB14) indicated (left), magnified images of

PhB1 to PhB14 and their corresponding reflection spectra (right), scale bar: 100 µm (left) and 20 µm (right) **c)** reflection spectra of a ZIF-8 photonic ball collected under constant EtOH atmosphere (P/P_0 = 0.25) with changing temperature from 25 to 50 ^oC, **d)** EtOH desorption isobars obtained via the shifts of the photonic band of the ZIF-8 photonic ball taken at P/P_0 = 0.25, 0.65 and 0.90. The bigger points correspond to the experimental data while the smaller dashes are the sigmoidal fit.

Further optical analysis on the other synthesized materials such as the ZIF-8/AuNP, ZIF-8/PVA and ZIF-67 balls demonstrated that all of the materials exhibited photonic properties (**Figure S10**, **Supporting Information**). However, we have chosen the simplest structure made of ZIF-8 photonic balls to continue for the application.

To investigate the possible applicability of the ZIF-8 photonic balls for thermal probing we built a customized environmental setup. The hyperspectral microscope was thus equipped with a thermal stage and an environmental chamber that allows injection of a gas flux containing a controlled relative vapor pressure (called here P/P_0) of solvent as depicted in **Figure 4a**. By this method, we could access the thermal-mediated physisorption properties of each individual ZIF-8 photonic ball in presence of alcohol vapors. In a first experiment, we created thermo-optical calibration curves. Samples were exposed to EtOH vapor with P/P_0 = 0.25 and the evolution of the reflection spectra was recorded by increasing the stage temperature from 25 °C to 50 °C (**Figure 4c)**. The shift of the photonic peak ($\Delta\lambda_{max}$) as function of the temperature was plotted in **Figure 4d** (blue curve)**.** In these conditions, at 25 °C, ZIF-8 micropores are completely filled with EtOH, and the photonic diffraction peak is centered at λ = 555 nm. By increasing the temperature, the EtOH is progressively desorbed from the microporosity causing a decrease of the refractive index of the ZIF-8 colloids. At 50 °C, ethanol desorption results in a blueshift of the photonic band of 26 nm. As displayed in **Figure 4d** the shift *vs* temperature evolution is not linear, but exhibits a steep increase around 40 ^oC (**Figure 4d**). This narrow temperature range of desorption observed is correlated with the homogeneous microporosity of ZIF-8 particles (pore size = 1.1 nm) and strongly depends on the EtOH relative pressure in the atmosphere. The same experiment was repeated by fixing the P/P_0 at 0.65 and 0.90 into the chamber. As expected, as shown in **Figure 4d** (red and black curves), a similar trend is observed but the desorption occurred at higher temperatures. All collected reflection spectra used for thermo-optical isobars reconstruction (corresponding to P/P_0 of 0.25, 0.65 and 0.90) are given in **Figure S11.** The photonic balls exhibit a similar behavior, which does not depend on the size, shape or distance between the balls. From an

applicative point of view, the ZIF-8 photonic balls in presence of vapors behave as individual thermal probe in which a local variation of temperature can be monitored by a λ_{max} shift. For a label-free material, its intrinsic sensitivity depends thus on the temperature-induced refractive index variation of the material that is defined by the so-called "thermo-optic coefficient" dn/dT. Based on refractive index values determined in previous studies[61] we can estimate that, in presence of 25% EtOH, the thermo-optic coefficient of ZIF-8 photonic balls is equal to $1*10^{-2}$ K^{-1} between 35 and 45°C. As a comparison, for materials already used in thermo-plasmonics, the dn/dT is of the order of 10^{-8} K^{-1} for SiO_2 and 10^{-4} K^{-1} for PMMA in the same temperature range. In addition, compared to mesoporous materials,[4] this system exhibits higher sensitivity in a narrow range of temperature thanks to the sharp physisorption capabilities of the microporous ZIF-8. In our case, the desorption temperature strongly depends on the EtOH vapor pressure. Interestingly, this property allows the fine tuning of temperature detection range between 25 and 60°C "on-demand" by simply switching P/P_0. This the range of interest for many common applications taking place at room temperature including heating in microelectonic devices or biological surfaces.

As proof of concept of application, we exploited the thermal probing capabilities of the ZIF-8 photonic balls to "map" thermal gradients at the sub-millimeter scale. To realize this, we induced formation of a "hot spot" by a concentrated laser beam. The experimental setup is shown in **Figure 5a**. We produced a glass substrate with a light absorbing layer that consisted of a PDMS + carbon black mixture. For the experiment, we spread the photonic powder over this substrate. Then we turned on the laser (diameter of the laser beam = 400 µm, 532 nm, 1 Watt, continuous) that was set underneath the sample and focalized on the region of interest using a dark field condenser (**Figure 5a**). We used an optical filter of 532 nm to prevent the laser beam to interfere with the acquisition of the reflection spectra and to protect the hyperspectral detector from oversaturation. We let the laser beam for at least 10 min to ensure the formation of a stable thermal gradient between the irradiated and non-irradiated parts of the substrate. Then, we selected four photonic balls to be used as thermal probes, that we called photonic probes. Named PhB_p1, PhB_p2 PhB_p3 and PhB_p4, these photonic probes were located at a respective distance of 0, 90, 310 and 450 µm from the center of the laser focalization spot (**Figure 5b**). We started acquiring hyperspectral images and reflection spectra from these photonic probes with EtOH relative pressure decreasing gradually from 1 to 0 (**Figure S12**, **Supporting Information**). **Figure 5c** highlights the measured $\Delta\lambda_{max}$ of the each of the four photonic balls at a selected P/P_0 (corresponding with the example in **Figure**

4d). The selected EtOH relative pressures were $P/P_0 = 0.25$ for PhB_p1 and PhB_p2, $P/P_0 = 0.65$ for PhB_p3 and $P/P_0 = 0.90$ for PhB_p4.

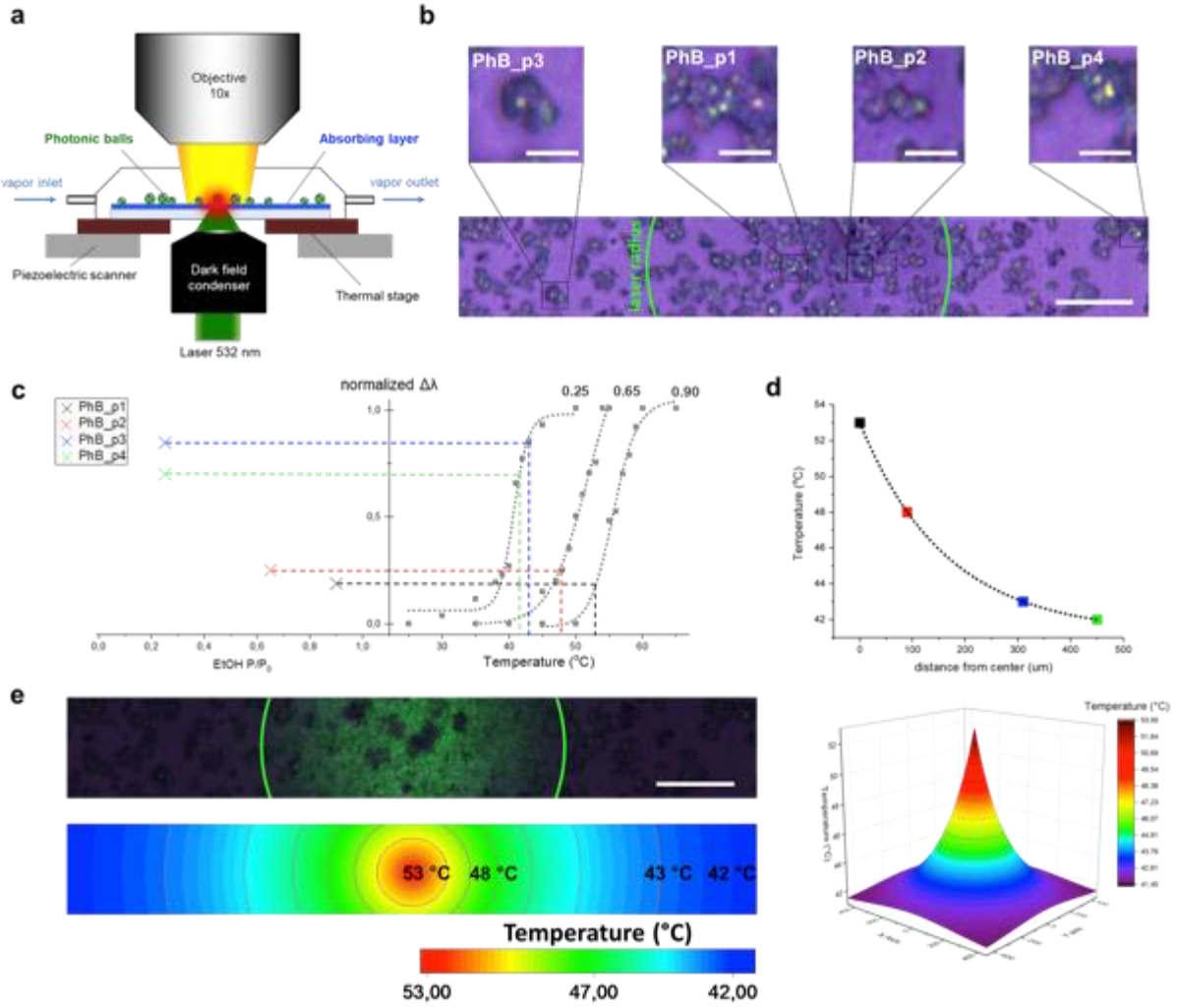

Figure 5. The thermal probing experiments. **a)** Scheme of the experimental setup. **b)** Hyperspectral image of the region of interest of the sample (bottom) and magnified images of the four photonic probes (top): PhB_p1, PhB_p2, PhB_p3 and PhB_p4, scale bars: 25 µm (top), 100 µm (bottom). **c)** Correlation study of the P/P_0 values of four photonic probes to their corresponding temperatures at fixed Δλ. The four crosses on the left represent the normalized Δλ values recorded at $P/P_0 = 0.25$ for PhB_p1 and PhB_p2, $P/P_0 = 0.65$ for PhB_p3 and $P/P_0 = 0.90$ for PhB_p4. The calibration desorption curves obtained at $P/P_0 = 0.25$, 0.65 and 0.90 and their corresponding sigmoidal fits are represented on the right. The colored vertical and horizontal dashed lines are added to help the visualization of the correlation between the P/P_0 and temperature**. d)** Temperature values plotted versus the distance of four photonic probes to the center of the laser irradiated area, the smaller dots represent the exponential decay fit. **e)** Hyperspectral and OM image of the region of interest

of the sample in superposition to show the laser irradiated area (up) and its corresponding thermal map in 2D (down) and 3D (right).

These measurements enabled correlating the $\Delta\lambda_{max}$ of the photonic probes with the desorption isobar calibration curves. The two plots are displayed side by side in **Figure 5c**. Correlating the two plots, we found the temperature for PhB_p1, PhB_p2, PhB_p3 and PhB_p4 being 53, 48, 43 and 42 ^{o}C, respectively. These values were then plotted with respect to their corresponding distances to the center of the laser focalization spot (**Figure 5d**). The plot conformed perfectly to an exponential decay function. These values represented the local temperatures on the substrate. Since the gradient is supposed to be radially isotropic around the laser beam, it can be displayed as a color-coded image to form a thermal gradient as expected from the focalized heating of the center of the substrate (**Figure 5e** and **Figure S13**, **Supporting Information**). Despite the simplicity of the geometry of the heating spot, this example illustrates the potential of using of MOF photonic balls for local thermal probing. As mentioned above, by this method we also prepared ZIF-67 photonic balls that combine the photonic colors due to the presence of the self-assembled superstructures with the intrinsic color that results from the strong absorption of Co species in ZIF-67. As another proof of concept, we demonstrated that, ZIF-67 photonic ball, we can act as local photothermal probes in which the photonic signal varies with the laser intensity (Figure S14, Supporting Information).. We exploited the photo-thermal heating capability of the cobalt-based ZIF-67 photonic balls to trigger the desorption of EtOH from the pores by simple laser irradiation. In this experiment, the ZIF-67 photonic balls (φ = 193 nm) were spread over a bare glass transparent substrate and exposed to EtOH at saturated vapor pressure. The pore empty and the pore full states of a single ZIF-67 photonic ball were characterized with the hyperspectral microscope (Figure S14, Supporting Information). Then, a photonic ball was irradiated with the 532 nm-laser by gradually increasing the power changing from 0 to 1 W. Interestingly, the photonic diffraction peak that was centered at λ = 537 nm at the pore full state shifted back to λ = 517 nm (pore empty state) at the laser power of 0.88 W (Figure S14, Supporting Information). The effect can be be quantified by a decrease in reflectance of 37% at a wavelength of 552 nm. This indicated that photonic balls made of a light absorbing MOF, ZIF-67, can be activated with laser irradiation and that the desorption of EtOH triggered by a photo-thermal can be tracked with the shift of the photonic diffraction peak. This result supports the generality of our method extending to different MOF materials with different physical capabilities and offers new concepts to the field of photonics.

Besides, compared to other MOF based optical structures (films or monoliths), photonic balls offer several advantages in terms of applicability and versatility: (i) they are discrete objects that do not cover entirely the allow local temperature probing by preserving a view of the underlying substrate; (ii) films or monolith need to be processed and assembled on the substrate of interest from liquid solution, a practical limitation in many relevant cases (biological surfaces, electronic devices, paper). MOF photonic balls are spray-dried powders and can be applied directly on any surface. As a further demonstration, we showed in **Figure S15**, **Supporting Information** that ZIF-8 photonic balls exhibiting different photonic colors could be applied directly on a leaf of poplar and that a photonic shift could be detected in presence of butanol vapors (as described above for EtOH). Interestingly, this experiment also suggests that, in perspective, MOF photonic balls could be used to detect organic molecules released from plants by phyto-volatilization. (iii) Once applied on a substrate, MOF photonic balls can be easily removed by an air-flux enabling recycling the surface/sample (**Figure S15**, **Supporting Information)**.

Beyond those advantages, it is important to underline that, as for all the thermal probes, this method is performing in certain conditions and present technical limitations. This can offer new directions for further developments and optimization. The sensitivity (photonic shift vs temperature) can certainly be enhanced by further improving the quality of the photonic structures or by using other guest molecules with higher refractive index. The detection range is of around 10-15°C for a given P/P_0 but, as explained above, it can be easily tuned "on-demand" by varing P/P_0 (that is far to be unpractical or costly). By using EtOH vapors the detection range is 25 and 60°C but it can be be extended toward higher temperatures by modifying the thermo-desorption characteristics. This can be done by (i) using other vapors (such as i-PrOH, BuOH etc.) or (ii) by fabricating micro-mesoporous photonic balls (such as based on MIL-101).

3. Conclusion

In summary, we demonstrate the first example of MOF photonic balls based on self-assembled colloidal particles and fabricated by a cost-effective and scalable spray drying process. This approach was mainly demonstrated for ZIF-8 but was also extended to other systems such as ZIF-67 and composite ZIF-8/Au NPs. By tuning the size of the colloidal building blocks, photonic balls exhibiting three different structural colors were prepared. A set of characterizations techniques was employed to investigate the structure, the morphology

and photonic properties at the single object level. SEM and X-Ray Nanotomography unveil that the final materials are composed of organized colloidal superstructures with various size, sphericity and morphology that are typical of the spray-drying process. Nevertheless, all the superstructures exhibit photonic properties as confirmed by Environmental Hyperspectral Microscopy analysis in which each single ball could be characterized independently and in controlled environmental conditions. By this study, we introduce a new concept of label-free temperature probing based on thermal-induced vapor sorption from micropores. We showed that, in presence of alcohol vapors, the MOF photonic balls could be used as thermal or photothermal probes to map local thermal gradients. Interestingly, by this approach the detected temperature range can be tuned "on-demand" by controlling the vapor pressure in the environment. This approach represents the first example of application of photonic MOFs not targeting chemical sensing. More generally, this method can be applied to other porous materials or other vapor molecules and can be potentially generalized to other optical methods to improve the thermal/spatial resolution. Beyond thermal sensing, MOF photonic balls could also find application in other fields as local chemical sensing, smart photonic pigments for paints or for anti-counterfeit.

4. Experimental Section

Materials: Zinc acetate dihydrate ($Zn(CH_3CO_2)_2 \cdot 2H_2O$), cobalt acetate tetrahydrate ($Co(CH_3CO_2)_2 \cdot 4H_2O$), 2-methylimidazole ($C_4H_6N_2$, 2-mim), poly(vinylalcohol) Mw = 13-23 kDa ($[\text{-}CH_2CHOH\text{-}]_n$, PVA), carbon black, tetrachloroauric acid trihydrate ($HAuCl_4 \cdot 3H_2O$), silver nitrate ($AgNO_3$), cetyltrimethylammonium bromide ($[(C_{16}H_{33})N(CH_3)_3]Br$, CTAB), cetyltrimethylammonium chloride solution (25% in water) ($[(C_{16}H_{33})N(CH_3)_3]Br$, CTAC), 1,1,3,3-tetramethylguanidine ($C_5H_{13}N_3$), Resorcinol ($C_6H_6O_2$), 8-hydroxyquinoline (C_9H_7NO), Ascorbic acid ($C_6H_8O_6$), citric acid monohydrate ($C_6H_8O_7 \cdot H_2O$), Sodium hydroxide (NaOH) were purchased from Sigma Aldrich. Sodium tetrahydroborate ($NaBH_4$) was purchased from Thermofisher. All chemicals were used without further purification.

Synthesis of ZIF-8 particles: The synthesis protocol of ZIF-8 particles with different sizes (φ = 184, 206, 242 and 275 nm) is adapted from the work of Avci *et al.*[61] After a typical synthesis, the resulting ZIF-8 particles were washed two times with an aqueous solution of CTAB (2.74 mM) and one time with DI water upon centrifugation at 9000 rpm in 50 ml Falcon tubes. The washed particles were finally re-dispersed in DI water at a concentration of 30 mg ml^{-1}.

Synthesis of ZIF-67 particles: $Co(CH_3CO_2)_2 \cdot 2H_2O$ (0.2 g) is dissolved in 5 ml of DI water. 2-mim (1.12 g for φ = 205 nm, 1.20 g for φ = 193 nm) is dissolved in 3 ml of DI water. 2.25 ml of an aqueous CTAB solution (2.74 mM) is added to the 2-mim solution. $Co(CH_3CO_2)_2 \cdot 2H_2O$ solution is added to the latter solution and the mixture is let at RT for 1h. The purple ZIF-67 crystals were washed two times with an aqueous solution of CTAB (2.74 mM) and one time with DI water upon centrifugation at 9000 rpm in 50 ml Falcon tubes. The washed particles were finally re-dispersed in DI water at a concentration of 30 mg ml^{-1}.

Synthesis of Au NPs: The synthesis protocol of Au NPs is adapted from the work of Chateau *et al*.[93] As a result, we obtained a concentrated, aqueous Au NP solution. (LSPR = 539nm and average diameter = 51 nm) The UV-Visible absorption spectrum and TEM micrograph of the Au NPs is in **Figure S16, Supporting Information**.

Preparation of colloidal solutions for spray drying: Typically, all the colloidal solutions to be spray dried were prepared in 10 ml batches in 30 mg ml^{-1} concentration. ZIF-8 and ZIF-67 colloidal solutions were used as synthesized. For ZIF-8/CB; 15 mg of carbon black is added to the ZIF-8 colloidal solution to obtain the mass ratio of CB:ZIF-8 = 5:100. This solution was vortexed thoroughly to obtain a homogeneous dispersion of CB. For ZIF-8/PVA; a negligible volume from an aqueous solution of PVA was added to the ZIF-8 colloidal solution to obtain the mass ratio PVA:ZIF-8 = 1:100. For ZIF-8/AuNP; 1 ml of the as-synthesized, concentrated, aqueous AuNP solution is added to 10 ml of ZIF-8 colloidal solution.

Spray drying: Photonic balls were assembled by spray drying, using the mini-spray drier B-290 supplied by Büchi. This setup operates in a "closed mode". The colloidal solution of interest is pumped *via* a peristaltic pump through the atomizer. A coaxial, hot air flow atomizes the suspension in droplets, which evaporate quickly leading to an aerosol of photonic balls composed of assembled MOF crystals. The aerosol passes through a glass cyclone and the MOF photonic balls are collected in a glass vial, while water vapor and by-products are passed through a filter and a dehumidifier. The air inlet temperature in the atomizer was set to 180 °C, the peristaltic pump rate to 3 mL min^{-1} and the air flow to 473 L h^{-1}.

General characterizations: Powder X-Ray diffraction was carried out using a D8 Advance diffractometer (Bruker), equipped with a Cu anode (Kα1 = 1.54056 Å and Kα2 = 1.54439 Å) and a 200 channels LynxEye detector. The measurements were collected in a range of 2θ spanning from 5° to 50°. Scanning electron microscopy (SEM) was carried out with a SU-70 Hitachi FESEM, equipped with a Schottky emission gun as source of electrons. The images were obtained with an accelerating voltage of 1kV and at a working distance of 10 mm.

X-Ray Nanotomography: The tomography data collection was carried out at the ANATOMIX beamline at synchrotron SOLEIL. The beamline uses a cryogenic in-vacuum undulator source (U18). The images were collected with a Hamamatsu Orca fiber detector, pixel size was 34.78 nm. The volume slices were reconstructed using PyHST 2 and analyzed using the Volume Viewer plug-in by ImageJ. Sample preparation: A steel needle is dipped gently in PDMS and the PDMS is let solidify for a few minutes. Then the photonic balls were deposed at the top of the PDMS covered steel needle and the sample is let at room conditions for 1 hour.

Alcohol desorption measurements: ZIF-8 photonic ball powder was carefully deposited on a plain glass slide with the help of a spatula by tilting the sample to remove the excess of photonic balls and obtain a monolayer of balls.. In this conditions, the great majority of the balls are directly touching the substrates . The few aggregates with multiple layers of photonic balls could be easily spotted and discarded because they were completely out of focus The sample is placed in a customized environmental chamber equipped with a gas flow and humidity controller (SOLGELWAY) and a temperature-controlled platform (Linkam Scientific). This chamber is then adapted to the sample stage of the hyperspectral microscope (CytoViva). Hyperspectral images constituting of 50 lines were acquired with an acquisition time of 0.250 s at each temperature that varied between 25 and 65 ^{o}C at EtOH P/P_0 of 0.25, 0.65 and 0.90.

Thermal Mapping Experiments: A similar setup to the alcohol desorption measurements was used with slight modifications. The photonic ball powder was carefully deposited on a light absorbing (black) substrate with the help of a spatula. The light absorbing substrate was prepared by coating a glass slide with a black paste composed of PDMS and carbon black mixed in 100:5 weight ratio. Then, this sample was placed in the environmental chamber and to the sample stage without the heating platform. A 532 nm, continuous, 1W green laser (Laserglow Technologies) was focalized to the sample in dark field transmission from underneath the sample. A 533 nm filter (Thorlabs) is used before the detector to prevent damaging and interfering with the spectral measurements. Hyperspectral images constituting of 150 lines were acquired with an acquisition time of 0.250 s at each EtOH P/P_0 values varying between 0 and 1.00.

AUTHOR INFORMATION

Corresponding Author

marco.faustini@sorbonne-universite.fr

Funding Sources

This work was supported by the European Research Council (ERC) under European Union's Horizon 2020 Programme (Grant Agreement no. 803220, TEMPORE).

ACKNOWLEDGMENT

We thank D. Montero and the Institut des Matériaux de Paris Centre (IMPC FR2482) for servicing FEGSEM & EDX instrumentation and Sorbonne Université, CNRS and C'Nano projects of the Région Ile-de-France for funding. We thank Mateusz Odziomek and Célia Aissani for their support on spray-drying. We thank Ryma Haddad for conducting the N_2 physisorption measurments. ANATOMIX is an Equipment of Excellence (EQUIPEX) funded by the Investments for the Future program of the French National Research Agency (ANR), project NanoimagesX, grant no. ANR-11-EQPX-0031. The nano-tomography data was collected during the SOLEIL inhouse proposal 99200044 and the user proposal 20191387. This experimental set-up was partially supported by the Paris–Ile-de-France Region, via the network of excellence DIM RESPORE.

5. References

[1] Q. Cheng, S. Rajauria, E. Schreck, R. Smith, N. Wang, J. Reiner, Q. Dai, D. Bogy, *Sci. Rep.* **2020**, *10*, 20087.

[2] G. Tessier, M. Bardoux, C. Boué, C. Filloy, D. Fournier, *Appl. Phys. Lett.* **2007**, *90*, 171112.

[3] M. Mecklenburg, W. A. Hubbard, E. R. White, R. Dhall, S. B. Cronin, S. Aloni, B. C. Regan, *Science* **2015**, *347*, 629.

[4] Z. Chehadi, C. Boissière, C. Chanéac, M. Faustini, *Nanoscale* **2020**, *12*, 13368.

[5] X. Tang, M. M. Ackerman, P. Guyot-Sionnest, *ACS Nano* **2018**, *12*, 7362.

[6] K. Okabe, N. Inada, C. Gota, Y. Harada, T. Funatsu, S. Uchiyama, *Nat. Comm.* **2012**, *3*, 705.

[7] K. Okabe, R. Sakaguchi, B. Shi, S. Kiyonaka, *Pflugers Arch - Eur J Physiol* **2018**, *470*, 717.

[8] A. Bednarkiewicz, J. Drabik, K. Trejgis, D. Jaque, E. Ximendes, L. Marciniak, *Appl. Phys. Rev.* **2021**, *8*, 011317.

[9] M. Dramićanin, In *Luminescence Thermometry* (Ed.: Dramićanin, M.), Woodhead Publishing, **2018**, pp. 215–233.

[10] Y. S. Ju, K. E. Goodson, *J Heat Transfer* **1998**, *120*, 306.

[11] C. Kousiatza, N. Chatzidai, D. Karalekas, *Sensors (Basel)* **2017**, *17*.

[12] O. S. Wolfbeis, *Chem. Soc. Rev.* **2015**, *44*, 4743.

[13] T. Chihara, M. Umezawa, K. Miyata, S. Sekiyama, N. Hosokawa, K. Okubo, M. Kamimura, K. Soga, *Sci. Rep.* **2019**, *9*, 12806.

[14] L. M. Maestro, E. M. Rodríguez, F. S. Rodríguez, M. C. I. la Cruz, A. Juarranz, R. Naccache, F. Vetrone, D. Jaque, J. A. Capobianco, J. G. Solé, *Nano Lett.* **2010**, *10*, 5109.

[15] C.-C. Fu, H.-Y. Lee, K. Chen, T.-S. Lim, H.-Y. Wu, P.-K. Lin, P.-K. Wei, P.-H. Tsao, H.-C. Chang, W. Fann, *PNAS* **2007**, *104*, 727.

[16] P. Bosch, F. Catalina, T. Corrales, C. Peinado, *Chem. Eur. J* **2005**, *11*, 4314.

[17] S. W. Allison, G. T. Gillies, A. J. Rondinone, M. R. Cates, *Nanotechnology* **2003**, *14*, 859.

[18] F. Vetrone, R. Naccache, A. Zamarrón, A. Juarranz de la Fuente, F. Sanz-Rodríguez, L. Martinez Maestro, E. Martín Rodriguez, D. Jaque, J. García Solé, J. A. Capobianco, *ACS Nano* **2010**, *4*, 3254.

[19] X. Rao, T. Song, J. Gao, Y. Cui, Y. Yang, C. Wu, B. Chen, G. Qian, *J. Am. Chem. Soc.* **2013**, *135*, 15559.

[20] Y. Cui, H. Xu, Y. Yue, Z. Guo, J. Yu, Z. Chen, J. Gao, Y. Yang, G. Qian, B. Chen, *J. Am. Chem. Soc.* **2012**, *134*, 3979.

[21] Y. Pan, H.-Q. Su, E.-L. Zhou, H.-Z. Yin, K.-Z. Shao, Z.-M. Su, *Dalton Trans.* **2019**, *48*, 3723.

[22] L. Li, Y. Zhu, X. Zhou, C. D. S. Brites, D. Ananias, Z. Lin, F. A. A. Paz, J. Rocha, W. Huang, L. D. Carlos, *Adv. Funct. Mater.* **2016**, *26*, 8677.

[23] G. Baffou, C. Girard, R. Quidant, *Phys. Rev. Lett.* **2010**, *104*, 136805.

[24] G. Baffou, M. P. Kreuzer, F. Kulzer, R. Quidant, *Opt. Express, OE* **2009**, *17*, 3291.

[25] Single Quantum Dots as Local Temperature Markers | Nano Letters **2007**, *7*, 3102

[26] P. Löw, B. Kim, N. Takama, C. Bergaud, *Small* **2008**, *4*, 908.

[27] P. Rodríguez-Sevilla, Y. Zhang, P. Haro-González, F. Sanz-Rodríguez, F. Jaque, J. G. Solé, X. Liu, D. Jaque, *Adv. Mater.* **2016**, *28*, 2421.

[28] D. Ross, M. Gaitan, L. E. Locascio, *Anal. Chem.* **2001**, *73*, 4117.

[29] M. Kondo, T. Yoshitomi, H. Matsuzaka, S. Kitagawa, K. Seki, *Angew. Chem., Int. Ed. Engl.* **1997**, *36*, 1725.

[30] H. Li, M. Eddaoudi, T. L. Groy, O. M. Yaghi, *J. Am. Chem. Soc.* **1998**, *120*, 8571.

[31] K. Barthelet, J. Marrot, D. Riou, G. Férey, *Angew. Chem., Int. Ed.* **2002**, *41*, 281.

[32] A. Kirchon, L. Feng, H. F. Drake, E. A. Joseph, H.-C. Zhou, *Chem. Soc. Rev.* **2018**, *47*, 8611.

[33] A. U. Czaja, N. Trukhan, U. Müller, *Chem. Soc. Rev.* **2009**, *38*, 1284.

[34] R. E. Morris, P. S. Wheatley, *Angew. Chem., Int. Ed.* **2008**, *47*, 4966.

[35] H. Li, K. Wang, Y. Sun, C. T. Lollar, J. Li, H.-C. Zhou, *Mat. Today* **2018**, *21*, 108.

[36] R. B. Getman, Y.-S. Bae, C. E. Wilmer, R. Q. Snurr, *Chem. Rev.* **2012**, *112*, 703.

[37] X. Li, X. Yang, H. Xue, H. Pang, Q. Xu, *J. Energy Chem.* **2020**, *2*, 100027.

[38] Z. Liang, R. Zhao, T. Qiu, R. Zou, Q. Xu, *J. Energy Chem.* **2019**, *1*, 100001.

[39] S. Zheng, Q. Li, H. Xue, H. Pang, Q. Xu, *Natl. Sci. Rev.* **2020**, *7*, 305.

[40] J. Liu, L. Chen, H. Cui, J. Zhang, L. Zhang, C.-Y. Su, *Chem. Soc. Rev.* **2014**, *43*, 6011.

[41] J. Lee, O. K. Farha, J. Roberts, K. A. Scheidt, S. T. Nguyen, J. T. Hupp, *Chem. Soc. Rev.* **2009**, *38*, 1450.

[42] Y.-S. Kang, Y. Lu, K. Chen, Y. Zhao, P. Wang, W.-Y. Sun, *Coord. Chem. Rev.* **2019**, *378*, 262.

[43] D. Farrusseng, S. Aguado, C. Pinel, *Angew. Chem., Int. Ed.* **2009**, *48*, 7502.

[44] Q. Wang, D. Astruc, *Chem. Rev.* **2020**, *120*, 1438.

[45] R. Zhu, J. Ding, J. Yang, H. Pang, Q. Xu, D. Zhang, P. Braunstein, *ACS Appl. Mater. Interfaces* **2020**, *12*, 25037.

[46] X. Li, J. Wei, Q. Li, S. Zheng, Y. Xu, P. Du, C. Chen, J. Zhao, H. Xue, Q. Xu, H. Pang, *Adv. Funct. Mater.* **2018**, *28*, 1800886.

[47] X. Jiang, L. Zhang, S. Liu, Y. Zhang, Z. He, W. Li, F. Zhang, Y. Shi, W. Lü, Y. Li, Q. Wen, J. Li, J. Feng, S. Ruan, Y.-J. Zeng, X. Zhu, Y. Lu, H. Zhang, *Adv. Opt. Mater.* **2018**, *6*, 1800561.

[48] Z.-G. Gu, A. Pfriem, S. Hamsch, H. Breitwieser, J. Wohlgemuth, L. Heinke, H. Gliemann, C. Wöll, *Microporous Mesoporous Mater.* **2015**, *211*, 82.

[49] Y. Zheng, F.-Z. Sun, X. Han, J. Xu, X.-H. Bu, *Adv. Opt. Mater.* **2020**, *8*, 2000110.

[50] G. Lu, J. T. Hupp, *J. Am. Chem. Soc.* **2010**, *132*, 7832.

[51] A. Lopez Aldaba, D. Lopez-Torres, C. Elosua, J.-L. Auguste, R. Jamier, P. Roy, F. J. Arregui, M. Lopez-Amo, *Sens. Actuator B-Chem.* **2018**, *257*, 189.

[52] H. Li, H. He, J. Yu, Y. Cui, Y. Yang, G. Qian, *Sci. China Chem.* **2019**, *62*, 987.

[53] J. W. M. Osterrieth, D. Wright, H. Noh, C.-W. Kung, D. Vulpe, A. Li, J. E. Park, R. P. Van Duyne, P. Z. Moghadam, J. J. Baumberg, O. K. Farha, D. Fairen-Jimenez, *J. Am. Chem. Soc.* **2019**, *141*, 3893.

[54] G. Zheng, S. de Marchi, V. López-Puente, K. Sentosun, L. Polavarapu, I. Pérez-Juste, E. H. Hill, S. Bals, L. M. Liz-Marzán, I. Pastoriza-Santos, J. Pérez-Juste, *Small* **2016**, *12*, 3935.

[55] Z. Zhao, Z. Zhang, C. Li, H. Wu, J. Wang, Y. Lu, *J. Mater. Chem. A* **2018**, *6*, 16164.

[56] G. Lu, O. K. Farha, W. Zhang, F. Huo, J. T. Hupp, *Adv. Mater.* **2012**, *24*, 3970.

[57] F. M. Hinterholzinger, A. Ranft, J. M. Feckl, B. Rühle, T. Bein, B. V. Lotsch, *J. Mater. Chem.* **2012**, *22*, 10356.

[58] O. Dalstein, E. Gkaniatsou, C. Sicard, O. Sel, H. Perrot, C. Serre, C. Boissière, M. Faustini, *Angew. Chem.* **2017**, *129*, 14199.

[59] O. Dalstein, D. R. Ceratti, C. Boissière, D. Grosso, A. Cattoni, M. Faustini, *Adv. Funct. Mater.* **2016**, *26*, 81.

[60] M. Tu, B. Xia, D. E. Kravchenko, M. L. Tietze, A. J. Cruz, I. Stassen, T. Hauffman, J. Teyssandier, S. De Feyter, Z. Wang, R. A. Fischer, B. Marmiroli, H. Amenitsch, A. Torvisco, M. de J. Velásquez-Hernández, P. Falcaro, R. Ameloot, *Nat. Mater.* **2021**, *20*, 93.

[61] C. Avci, I. Imaz, A. Carné-Sánchez, J. A. Pariente, N. Tasios, J. Pérez-Carvajal, M. I. Alonso, A. Blanco, M. Dijkstra, C. López, D. Maspoch, *Nat. Chem.* **2018**, *10*, 78.

[62] L. Bai, Y. He, J. Zhou, Y. Lim, V. C. Mai, Y. Chen, S. Hou, Y. Zhao, J. Zhang, H. Duan, *Adv. Opt. Mater.* **2019**, *7*, 1900522.

[63] I. Stassen, N. Burtch, A. Talin, P. Falcaro, M. Allendorf, R. Ameloot, *Chem. Soc. Rev.* **2017**, *46*, 3185.

[64] N. Vogel, S. Utech, G. T. England, T. Shirman, K. R. Phillips, N. Koay, I. B. Burgess, M. Kolle, D. A. Weitz, J. Aizenberg, *PNAS* **2015**, *112*, 10845.

[65] J. H. Moon, G.-R. Yi, S.-M. Yang, D. J. Pine, S. B. Park, *Adv. Mater.* **2004**, *16*, 605.

[66] Y. Zhao, X. Zhao, J. Hu, M. Xu, W. Zhao, L. Sun, C. Zhu, H. Xu, Z. Gu, *Adv. Mater.* **2009**, *21*, 569.

[67] J. Wang, C. F. Mbah, T. Przybilla, B. Apeleo Zubiri, E. Spiecker, M. Engel, N. Vogel, *Nat. Commun.* **2018**, *9*, 5259.

[68] M. Sakai, H. Kim, Y. Arai, T. Teratani, Y. Kawai, Y. Kuwahara, K. Abe, Y. Kuwana, K. Ikeda, K. Yamada, Y. Takeoka, *ACS Appl. Nano Mater.* **2020**, *3*, 7047.

[69] S.-H. Kim, S.-J. Jeon, G.-R. Yi, C.-J. Heo, J. H. Choi, S.-M. Yang, *Adv. Mater.* **2008**, *20*, 1649.

[70] H. Li, H. Wang, A. Chen, B. Meng, X. Li, *J. Mater. Chem.* **2005**, *15*, 2551.

[71] J. Wang, U. Sultan, E. S. A. Goerlitzer, C. F. Mbah, M. Engel, N. Vogel, *Adv. Funct. Mater.* **2020**, *30*, 1907730.

[72] G. Jacucci, B. W. Longbottom, C. C. Parkins, S. A. F. Bon, S. Vignolini, *J. Mater. Chem. C* **2021**, *9*, 2695.

[73] Y. Zhao, L. Shang, Y. Cheng, Z. Gu, *Acc. Chem. Res.* **2014**, *47*, 3632.

[74] M. Pang, A. J. Cairns, Y. Liu, Y. Belmabkhout, H. C. Zeng, M. Eddaoudi, *J. Am. Chem. Soc.* **2013**, *135*, 10234.

[75] X. Cai, X. Deng, Z. Xie, S. Bao, Y. Shi, J. Lin, M. Pang, M. Eddaoudi, *Chem. Commun.* **2016**, *52*, 9901.

[76] L. Lupica-Spagnolo, D. J. Ward, J.-J. Marie, S. Lymperopoulou, D. Bradshaw, *Chem. Commun.* **2018**, *54*, 8506.

[77] J. Troyano, A. Carné-Sánchez, C. Avci, I. Imaz, D. Maspoch, *Chem. Soc. Rev.* **2019**, *48*, 5534.

[78] C. Avci, Y. Liu, J. A. Pariente, A. Blanco, C. Lopez, I. Imaz, D. Maspoch, *Small* **2019**, *15*, 1902520.

[79] A. Carné-Sánchez, I. Imaz, M. Cano-Sarabia, D. Maspoch, *Nat. Chem.* **2013**, *5*, 203.

[80] C. Boissiere, D. Grosso, A. Chaumonnot, L. Nicole, C. Sanchez, *Adv. Mater.* **2011**, *23*, 599.

[81] H. Xu, Z. Tan, H. Abe, M. Naito, *J Ceram Soc JPN* **2011**, *119*, 180.

[82] R. Vehring, *Pharm Res* **2008**, *25*, 999.

[83] L. C. Chow, L. Sun, B. Hockey, *J Res Natl Inst Stand Technol* **2004**, *109*, 543.

[84] W. S. Cheow, S. Li, K. Hadinoto, *Chem Eng Res Des* **2010**, *88*, 673.

[85] A. G. Marquez, P. Horcajada, D. Grosso, G. Ferey, C. Serre, C. Sanchez, C. Boissiere, *Chem. Commun.* **2013**, *49*, 3848.

[86] H. M. Lisboa, M. E. Duarte, M. E. Cavalcanti-Mata, *Food Bioprod. Process.* **2018**, *107*, 49.

[87] S. Poozesh, E. Bilgili, *Int. J. Pharm.* **2019**, *562*, 271.

[88] T. A. G. Langrish, D. F. Fletcher, *Chem. Eng. Process.* **2001**, *40*, 345.

[89] K. Kida, M. Okita, K. Fujita, S. Tanaka, Y. Miyake, *CrystEngComm* **2013**, *15*, 1794.

[90] C. Avci, J. Ariñez-Soriano, A. Carné-Sánchez, V. Guillerm, C. Carbonell, I. Imaz, D. Maspoch, *Angew. Chem., Int. Ed.* **2015**, *54*, 14417.

[91] M. Scheel, J. Perrin, F. Koch, V. Yurgens, V. L. Roux, J.-L. Giorgetta, K. Desjardins, C. Menneglier, S. Zhang, C. Engblom, Y.-M. Abiven, G. Cauchon, C. Bourgoin, A. Lestrade, T. Moreno, F. Polack, C. David, T. Weitkamp, *Microsc. Microanal.* **2018**, *24*, 246.

[92] T. Weitkamp, M. Scheel, J. L. Giorgetta, V. Joyet, V. L. Roux, G. Cauchon, T. Moreno, F. Polack, A. Thompson, J. P. Samama, *J. Phys.: Conf. Ser.* **2017**, *849*, 012037.

[93] D. Chateau, A. Desert, F. Lerouge, G. Landaburu, S. Santucci, S. Parola, *ACS Appl. Mater. Interfaces* **2019**, *11*, 39068.